



Article

Electrochemical Assessment of As-Deposited $\text{Co}(\text{OH})_2$ by Electrochemical Synthesis: The Effect of Synthesis Temperature on Performance

Vladimir Parra-Elizondo ¹, Ana Karina Cuentas-Gallegos ², Beatriz Escobar-Morales ¹, José Martín Baas-López ¹, Jorge Alonso Uribe-Calderón ³ and Daniella Esperanza Pacheco-Catalán ^{1,*}

¹ Unidad de Energía Renovable, Centro de Investigación Científica de Yucatán, A.C. Carretera Sierra Papacal-Chuburná Puerto Km 5, Sierra Papacal, 97302 Mérida, Yucatán, Mexico; vparra88@hotmail.com (V.P.-E.); beatriz.escobar@cicy.mx (B.E.-M.); jose.baas@cicy.mx (J.M.B.-L.)

² Instituto de Energías Renovables, Universidad Nacional Autónoma de México, Priv. Xochicalco S/N Temixco, 62580 Morelos, Mexico; akcg@ier.unam.mx

³ Unidad de Materiales, Centro de Investigación Científica de Yucatán, A.C. Calle 43 No. 130 x 32 y 34 Col. Chuburná de Hidalgo, 97205 Mérida, Yucatán, Mexico; jorge.uribe@cicy.mx

* Correspondence: dpacheco@cicy.mx

Received: 8 October 2019; Accepted: 2 November 2019; Published: 7 November 2019



Abstract: In this paper, the influence of an electrolytic temperature bath was used in the electrodeposition process on the size, color, and shape of the as-deposited $\text{Co}(\text{OH})_2$, and the electrochemical performance was investigated. Three different temperatures of 25, 60, and 95 °C were evaluated for the electrodeposition of $\text{Co}(\text{OH})_2$ on stainless steel plates (SSP). The electrochemical performance of the as-deposited electrodes (SSP) was measured in a symmetric electrochemical cell (EC) arrangement. XRD, SEM, and N_2 physisorption analyses were carried out to evaluate the structure and morphological composition, along with the textural properties. Results showed that the hexagonal platelet micro-clusters of $\text{Co}(\text{OH})_2$ are formed in a mixed composition of both α - $\text{Co}(\text{OH})_2$ and β - $\text{Co}(\text{OH})_2$ phases, with the α - $\text{Co}(\text{OH})_2$ phase being the major phase formed in the electrodeposition process at temperatures below 95 °C, as suggested by the XRD analysis. Electrochemical cell performances were evaluated by galvanostatic cycling, results showed maximum areal capacity values of 1.97, 2.69, and 4.34 mA h cm^{-2} at a charge/discharge current of 6.25 mA cm^{-2} , for the as-deposited materials at 25, 60 and 95 °C, respectively. The specific power of the EC reached up to 19 kW kg^{-1} for the EC obtained material at 60 °C, with a specific energy of 2.8 W h kg^{-1} . The maximum specific energy was reached at a current density of 6.25 mA cm^{-2} , with a value of 10.79 W h kg^{-1} for the EC at 60 °C. These results offer some insight into how the morphology and composition of thin films can be tuned by the electrochemical synthesis temperature, yielding different electrochemical performances and areal capacity behaviors.

Keywords: electrochemical synthesis; cobalt hydroxide; morphology control; electrochemical performance; energy storage devices

1. Introduction

In order to meet the energy requirements for the future, better management and utilization of electrical energy resources are needed. Energy storage systems offer a solution in terms of harvesting energy from intermittent renewable sources, such as eolic and photovoltaic, which nowadays are among the most robust technologies offering energy storage solutions. Eventually, the advances in energy storage technologies, such as in batteries and electrochemical capacitors, will ease the transition

of renewable energy sources into the electrical grid for their portability. Electrochemical capacitors are known to be efficient in power density over the batteries and significant cyclability performance [1]. Despite those advantages, electrochemical capacitors present a significant disadvantage in terms of their energy-density output over the batteries [2]. To overcome energy-density limitations, a strategy shown in numerous studies has been the evaluation of different types of electrode materials, such as electroconductive polymers [3], metal oxides [4,5], and metal hydroxides [6], even mixtures of oxides combining architectures of different morphologies [7,8]. One approach to overcome energy density disadvantages in electrochemical storage technologies is using transitional metal hydroxides or oxides that can be obtained by several methodologies such as chemical vapor deposition [9] or a hydrothermal process [10]. Another approach is combining materials with high specific surface area and high-energy-density materials [11]. The main feature of this type of energy-density enhancer arises in the chemical process in which Faradaic contributions can increase energy density since the redox process occurs at specific potentials in which the composite can be reduced or oxidized, limiting the operation of the electrochemical cell in order to enhance performance.

It is essential to mention that those redox processes lead by a Faradic contribution need to be stable in terms of cycling stability, thus the importance to search for a stable electrochemical performance in electrochemical capacitor materials [12]. Among the studied metal oxides, ruthenium oxide exhibits excellent behavior in terms of electrochemical performance due to its high specific capacity, as given by redox reactions in the charge/discharge process [13], maintaining nearly a constant current in voltammetric analysis among the potential window. However, due to its high cost, the use of this material in energy applications is limited.

However, cobalt hydroxide offers a solution as a cost-effective material for energy storage materials due to their layered structure, with interlayer spacing for fast ion insertion/desertion. $\text{Co}(\text{OH})_2$ is mainly used as an additive to increase the electrochemical activity of alkaline batteries and presents excellent electrochemical capacitance performance and well-defined behavior [14]. Moreover, the possibility of enhanced performance through different synthesis methods, such as hydrothermal [15], chemical precipitation [16], and electrochemical deposition [17], have also made it very viable for energy-storage applications as the active material in electrode storage devices.

Electrochemical deposition synthesis exhibits several advantages over the main synthesis processes presented in the literature, such as chemical precipitation and hydrothermal routes [10]. These advantages can be mentioned as being a one-step process with a low risk of operation by hazardous conditions (temperature, pressure), selective electrodeposition over conductive substrates, and tunable control over the variables present in the electrodeposition process (temperature, time, concentration).

Throughout the literature, several reports about the electrochemical deposition of $\text{Co}(\text{OH})_2$ evaluating the capacitive performance are presented. Gupta et al. [18] have reported a potentiostatic electrodeposition process of nanostructured $\alpha\text{-Co}(\text{OH})_2$ with a specific capacitance of 860 F g^{-1} (conversion made with the given information by the reference for about $2.48 \text{ mA h cm}^{-2}$ of areal capacity, nominal potential window of 0.4, electrodeposited mass density of 0.8 mg cm^{-2} and a total electrode surface area of 48 cm^2 in a three-electrode cell configuration). A two-electrode cell configuration capacitance of 44 F g^{-1} ($1.62 \text{ mA h cm}^{-2}$) was reported by Jagadale et al. [19] by potentiodynamic electrodeposition of $\text{Co}(\text{OH})_2$ onto stainless steel plates at 300 K at a low current charge of 5 mA at a potential window of 1.2 V. For galvanostatic electrodeposition, the material presented by Aghazadeh et al. [20] at a low electrodeposition bath temperature of 10°C exhibited a specific capacitance of 736 F g^{-1} ($47.7 \text{ mA h cm}^{-2}$), which was determined by cyclic voltammetry at a scan rate of 100 mV s^{-1} in a 0.7 V window for 1 g cm^{-2} in a three-electrode cell configuration.

Since morphology control is a significant difficulty to overcome in traditional chemical precipitation synthesis, along with the use of surfactants as templates increasing the operation cost, a search for a rapid and controllable surface growth synthesis process to produce redox-type materials for electrochemical energy storage applications is needed. However, there are only a few reports that compare the effect of

microstructural modification by the electrolytic bath temperature on the electrochemical performance of the $\text{Co}(\text{OH})_2$.

This work is focused on the electrodeposition morphology products and how the electrolytic bath temperature (25, 60, and 95 °C) affects the charge storage in the electrodeposition process in terms of the size, color, and shape of the obtained as-deposited coated SSPs.

2. Materials and Methods

All chemicals were used as received, the cobalt (II) nitrate hexahydrate $\text{Co}(\text{NO}_3)_2 \cdot 6 \text{H}_2\text{O}$ and potassium hydroxide KOH were obtained from Sigma-Aldrich. Solutions were prepared using deionized water.

2.1. Synthesis by Electrochemical Deposition

Electrochemical deposition synthesis started with the preparation of the 316 stainless steel plates (SSP) substrates. The SSPs were cleaned with detergent, deionized water, ethanol, and acetone, respectively. The cleaned SSPs (4 cm × 4 cm) were used as substrates in the electrodeposition of $\text{Co}(\text{OH})_2$ films. The counter and reference electrodes were stainless steel mesh (16 cm × 16 cm) and a standard calomel electrode (SCE), respectively. An aqueous solution of 0.1 M $\text{Co}(\text{NO}_3)_2 \cdot 6\text{H}_2\text{O}$ was used as an electrolyte and electrodeposition precursor. The three electrodes were immersed in the solution at the reaction chamber. Then, the vessel was submerged into a glycerin bath with magnetic stirring over a hot plate, adjusting the temperature control until the electrolytic temperature reached the equilibrium at 25, 60, and 95 °C. The temperature was monitored inside the electrochemical chamber with a thermometer rod inside the electrodeposition precursor solution. The electrodeposition continued until there were no changes in the temperature media for 10 min. The film was obtained via a chronopotentiometry by applying -1.16 mA cm^{-2} for 20 min using a Biologic VSP potentiostat. After the electrodeposition process, the as-electrodeposited $\text{Co}(\text{OH})_2$ films on a SSP substrate were washed several times using deionized water and dried in an oven at 40 °C overnight.

2.2. Characterization of the As-Deposited Materials

The characterization of the as-deposited $\text{Co}(\text{OH})_2$ was evaluated by morphological, physicochemical, and electrochemical techniques. The morphology was studied by scanning electron microscopy (SEM) with a JEOL JSM-7001F microscope, and elemental analysis (EDX) was performed with a detector coupled to SEM. The X-ray diffraction patterns (XRD) of the as-deposited materials were obtained using a Bruker D8 Advance, with a diffraction angle (2θ) from 10 to 80°. N_2 adsorption/desorption isotherms were performed to determine the textural properties of the materials obtained; samples were collected from powders scraped off the electrodeposits. Quantachrome Nova 2200 Surface Analyzer was used to perform the analysis. BET calculations to determine the surface area and the BJH method from the NovaWin[®] 11.03 software (Quantachrome Instruments, Boynton Beach, Florida, USA) to determine the pore size distribution were applied.

2.3. Electrochemical Characterization of the As-Deposited Materials

Symmetric cells were assembled with stainless steel plates as the current collector and the electrodeposited materials to evaluate the behavior of $\text{Co}(\text{OH})_2$ capacitive properties. Each electrode had an area of 16 cm^2 and was pressed together between two acrylic plates, with a filter paper that served as the separator. The cell was then immersed in 1 M KOH solution as the electrolyte. The electrochemical properties of symmetric $\text{Co}(\text{OH})_2$ - $\text{Co}(\text{OH})_2$ cells were studied in a two-electrode cell assemble, along with the electrochemical performance of as-deposited materials in a three-electrode cell arrangement to evaluate redox potentials. The characterization consisted of cyclic voltammetry tests after initial electrochemical activation at a scan rate of 1 mV s^{-1} for five sweep cycles in a potential window from 0 to 1 V, determined by the electrolyte KOH 1 M. Then, cyclic voltammetry was performed at different scan rates from 5 to 100 mV s^{-1} . Specific power and energy density were calculated through

galvanostatic charge/discharge cycling using Equations (3) and (4). The test was performed in a range of currents from 6.25 mA cm^{-2} to 62.5 mA cm^{-2} . The electrochemical performance was calculated using Equation (1) for a cell capacitance calculation.

$$C_{sp} = \frac{I t_d}{\Delta E_d a m} \quad (1)$$

where C_{sp} , corresponds to the specific capacitance in a symmetric cell arrangement, I , equals the current, t_d equals the discharge time, ΔE_d is equivalent to the potential interval in which the discharge process takes place, and a agrees with the geometric area of the electrode. The mass of the as-deposited material is represented by m . Equation (2) was used to calculate the equivalent series resistance (ESR).

$$ESR = \frac{\Delta E_c}{2I} \quad (2)$$

where ΔE_c corresponds to the maximum charge potential value in the evaluated window potential, and I , matches with the charging current of the device. Equations (3) and (4) were used to calculate the energy and power density for the ECs through galvanostatic charge/discharge.

$$E_{sp} = \frac{C \Delta E^2}{2} = \frac{C (E_{max} - E_{min})^2}{2} \quad (3)$$

$$P_{sp} = \frac{\Delta E}{4 ESR} = \frac{(E_{max} - E_{min})}{2} \quad (4)$$

where C corresponds to the cell capacitance C_{sp} from Equation (1), and ΔE is equivalent to the voltage window limited by the aqueous electrolyte. Finally, potentiostatic electrochemical impedance spectroscopy (PEIS) tests were performed at 0 V against an open circuit potential (OCP) in a frequency range from 200 kHz to 10 mHz, with a sinus amplitude of 10 mV to determine the equivalent series resistance of the assembly and elucidate an equivalent circuit in which the components can be associated with quantitative variables.

3. Results

3.1. Electrochemical Synthesis of Co(OH)_2

Figure 1 shows typical species concentration patterns in chronopotentiograms, where they can be seen as an increase in the recorded potential as the temperature increases in the electrochemical synthesis. The potential shift between samples arises from the thermal energy contribution in the electrolyte, which promotes a faster formation of OH^- species in the electrode–electrolyte interface, lowering the energy requirement for electro-base generation in the deposition process. Similar curves are shown by Zhou et al. [21] using chronoamperograms by assisted surfactant electrosynthesis, exhibiting the initial change of concentrations in the electrogenerated species on the electrode surface. The average electrodeposited mass loading of Co(OH)_2 on the SSP substrate was 0.7 mg cm^{-2} .

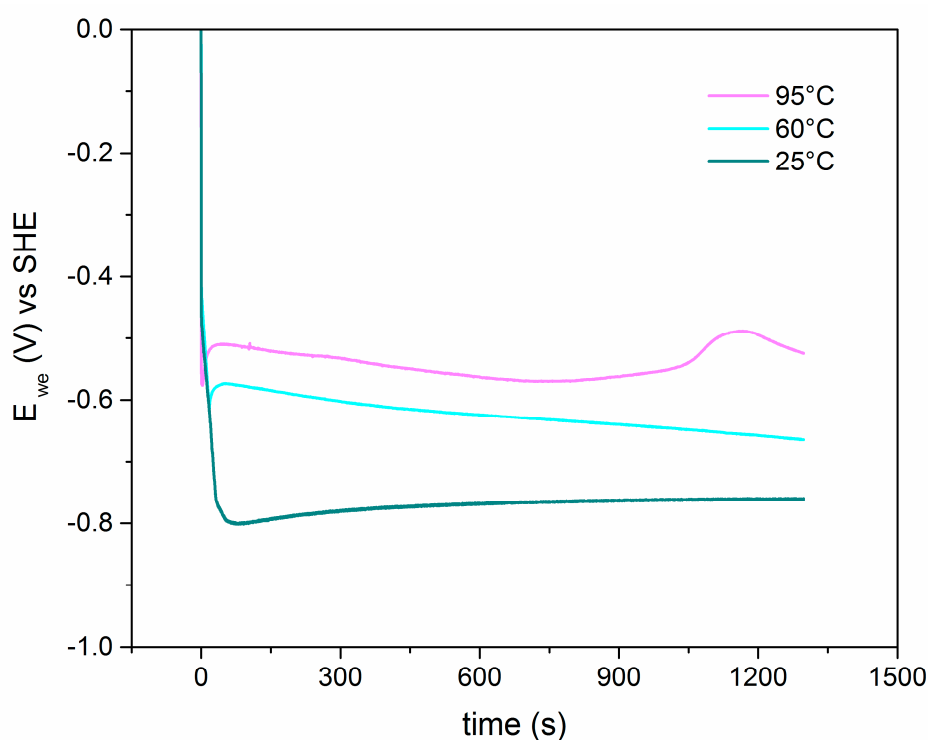
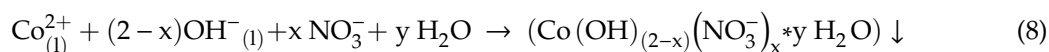
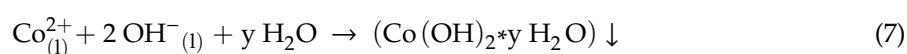
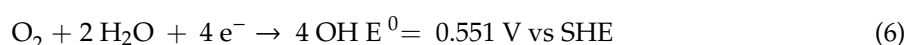


Figure 1. Electrodeposit chronopotentiograms plots at different temperatures in 0.1 M $\text{Co}(\text{NO}_3)_2$.

The electrochemical synthesis can be represented as a two-process step. The first step is associated with an OH^- electrogeneration over the interface of the electrode/substrate, as suggested by reactions (5) and (6), followed by Co ion precipitation due to complexation with the high concentration of OH^- as a result of the polarization in the electrode–electrolyte interface, as shown by the electrochemical precipitation reactions (7) and (8) [22]. The intermediate steps between reactions suggest the path to ion insertion in the hydroxyl matrix of the as-deposited materials, in this case, the NO_3^- .

Electrodeposition process:



Along with the potential increase response, a color change in the SSP electrodes can be observed in Figure 2, changing from a bluish color deposit, characteristic of $\alpha\text{-Co}(\text{OH})_2$, for the as-deposited materials at 25 and 60 °C to a light pink color, typical of $\beta\text{-Co}(\text{OH})_2$, when the as-deposited material was made at 95 °C. All as-deposited electrodes were resistant to several distilled water and ethanol rinses, presenting strong adhesion.

The size, shape and color of the electrodeposit is directly correlated to nuclei growth kinetics and the thermodynamic process in electrodeposition, in which the involved nucleation of species interacts on the vicinity of the electrode/electrolyte interface. This process is firmly time-dependent, in which the gradual growth increases, generating an overlap in the nuclei sites. These nuclei sites are influenced by the lattice orientation in the substrate and specific free surface in the vicinity of the electrode/electrolyte [23].

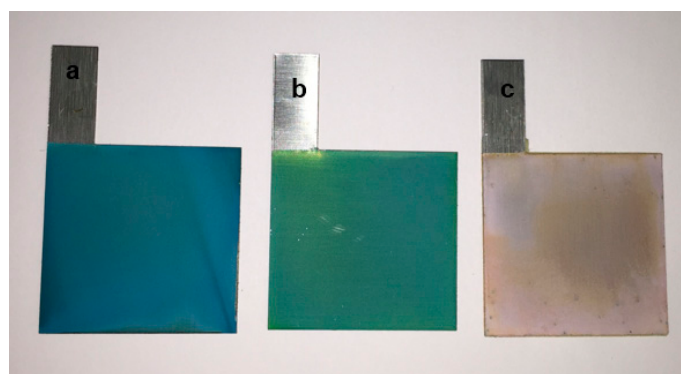


Figure 2. As-deposited stainless steel electrodes obtained at (a) 25 °C, (b) 60 °C, and (c) 95 °C.

Diffraction planes of the as-deposited Co(OH)_2 on to stainless steel current collectors are shown in Figure 3. As-deposited powders show diffraction plane signals for (001), (100), (011), (012), (111), and (311) located at 19.06° , 32.5° , 38.05° , 51.41° , 58.3° , and 62.7° , respectively, that can be attributed to $\beta\text{-Co(OH)}_2$ according to crystallographic data sheet, JCPDS 74-1057 [24]. The presence of additional diffraction signals for the (003) and (006) planes located at 11.35° and 33.05° in the diffractogram of the as-deposited material at 95 °C suggests—by the displacement to higher diffraction angles—the formation of mixed phases between rhombohedral α - and octahedral $\beta\text{-Co(OH)}_2$, since the diffraction signals in the low- and mild-temperature materials are not broadened in the as-deposited materials at 25 and 60 °C [25]. In general, the displacement to a small-diffraction-angle planes can be associated with the intercalation of NO_3^- in the as-deposited materials obtained at 25 and 60 °C as the interplanar distance is nearly doubled in the c-axis of the unit cell.

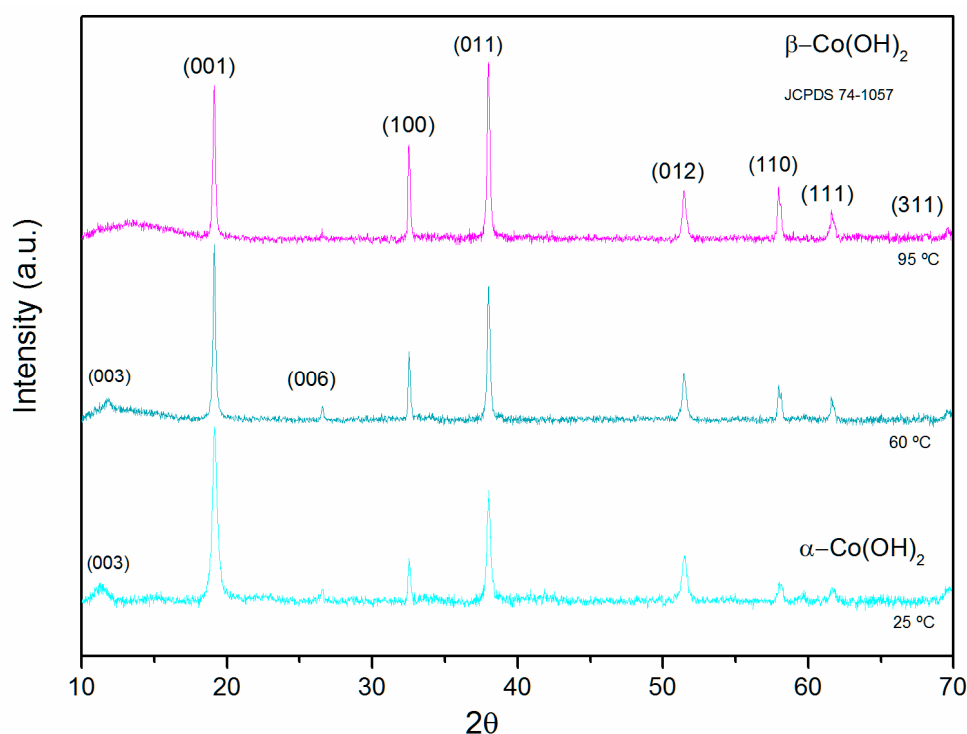


Figure 3. XRD patterns of the as-prepared Co(OH)_2 films.

Table 1 shows the calculated interplanar distance Equation (9), and crystallite size by Scherrer Equation (10), the ratio of those diffraction parameters can be associated with the number of layers in the crystallite cell, according to Dam et al. [26]. The uniformity of lattice strain in a certain aligned direction

can modify the d-spacing, and when these phenomena occur, an increase in the interplanar space will be seen as a diffraction signal shifts to lower diffraction angles, as seen in the low-temperature samples obtained at 25 and 60 °C. When the d-spacing is reduced by synthesis procedures, the diffracted signals shift to higher diffraction angles, explaining the broadening of the diffraction plane (003) in the as-deposited material at 95 °C.

Table 1. Analysis data from XRD characterization.

Sample (Lattice)	d (Å)	B (rad)	L (Å)	Layers (L d ⁻¹)
25 °C (003)	7.8	6.49×10^{-3}	218	28
60 °C (003)	7.5	3.53×10^{-3}	401	53
95 °C (001)	4.6	4.00×10^{-3}	375	81

$$2d \sin \theta = n\lambda \quad (9)$$

$$L = \frac{K \lambda}{B \cos \theta} \quad (10)$$

The increase of the temperature, in the 95 °C as-deposited sample, showed three-times more intrinsic layers in the crystalline cell compared to the as-deposited material at 25 °C, and up to almost two-times the calculated number of layers obtained in the electrochemical deposits made at 60 °C. This increase in the number of intrinsic layers is associated with the reduction of the interplanar space of the crystal cell, thus, limiting the intercalation of water and ion molecules inside the crystalline cell. As for the other two mixed phases present in the deposits obtained at 25 and 60 °C, the calculated values of the interplanar distance between layers suggests an increase of the space produced by the ion insertion in the double-layer hydroxalate-type of α -Co(OH)₂.

The SEM images of the electrodeposit obtained by chronopotentiometry are presented in Figure 4 for the three synthesis temperatures (25, 60, and 95 °C). The morphology of electrodeposition performed at 25 °C shows coral-like clusters; this cluster type of shape is similar to that reported by Kong et al. [27], obtained by chronoamperometry at a potential of −1 V vs. SCE. With a temperature increase from 60 to 95 °C, the electrodeposited material shows a domain reduction with a distinctive hexagonal platelet form in the hollow arrangement; similar structures were obtained by Aghazadeh et al. [28] by galvanostatic deposition. The hexagonal platelet clusters showed a reduction in size with smaller-size domains when the synthesis temperature was 95 °C. These results are in agreement with the XRD section in which the increase in temperature inferred a higher crystallinity in the as-deposited materials.

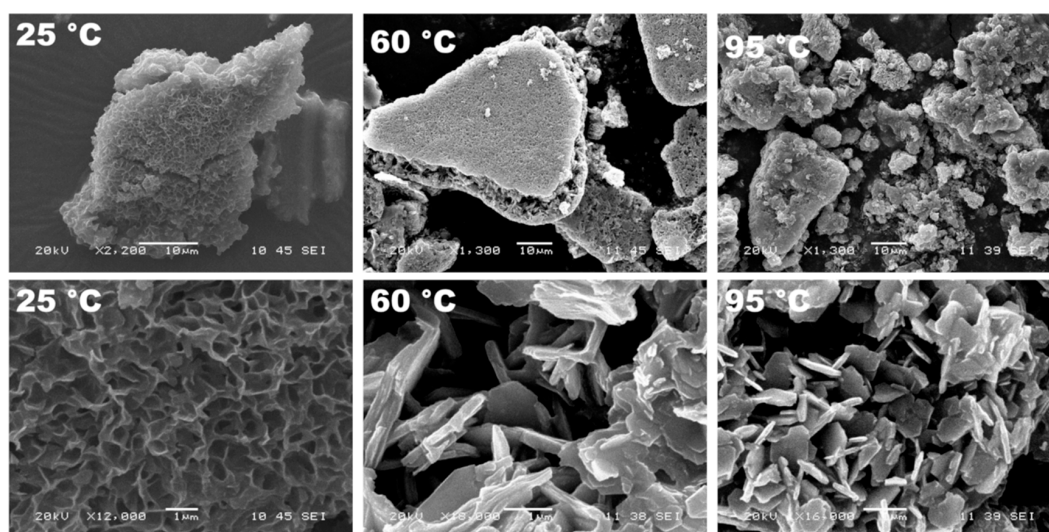


Figure 4. The microstructure of as-deposited Co(OH)₂ at different temperatures.

Changes in the morphology of the as-deposited materials can be associated with the Co^{2+} ion mobility by the thermodynamic energy changes and energy, thus increasing the rate of transport of the Co^{2+} ions towards the electrode surface [29]. Along with these changes in size, a different type of deposit forms when the temperature is increased in samples at 60 and 95 °C, changing from a type of coral-like structure to a platelet-cluster formation. Moreover, the observed changes in the as-deposited material from a bluish to a pink film suggests a change in Co composition.

EDX analysis is presented in Figure 5 as the spectrum shows the highest contribution in the material is for O_2 . As temperature increases in the electrochemical deposition process, this percentage reduces by nearly five percent. In Table 2, the results of the collected data are presented. It can be seen that the decrease in O_2 is given by the reduction of the layered double hydroxides (LDH) material, limiting the degree of OH^- insertion and nitrate ions adsorbed in the interlaminar space.

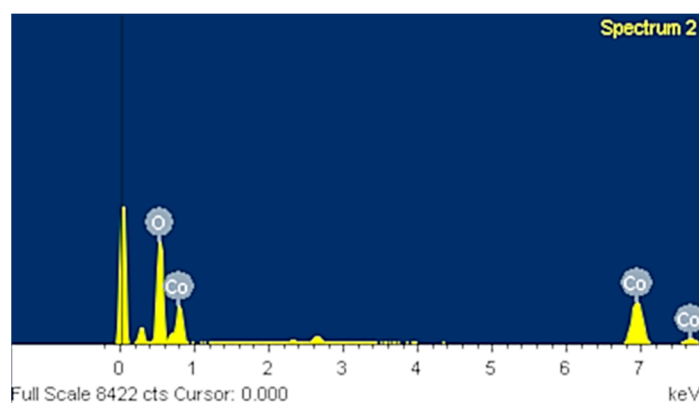


Figure 5. Elemental analysis (EDX) spectrum of the electrodeposited $\text{Co}(\text{OH})_2$ (initial signals attributed to carbon tape used in the analysis).

Table 2. EDX analysis.

Sample	Weight %		Atomic %	
	Co	O_2	Co	O_2
25 °C	54.56	45.44	24.70	75.30
60 °C	56.77	43.24	26.29	73.71
95 °C	59.04	40.96	28.30	71.70

Textural properties analysis by N_2 adsorption/desorption isotherms is presented in Figure 6, in which adsorption/desorption isotherms present a type-IV shape according to the IUPAC classification, which is common in mesoporous materials. An H-2 hysteresis cycle was observed, which is typically a signal of weak interactions between N_2 and $\text{Co}(\text{OH})_2$, this weak interaction can be associated with the interconnectivity of the pores between the adsorbent structures.

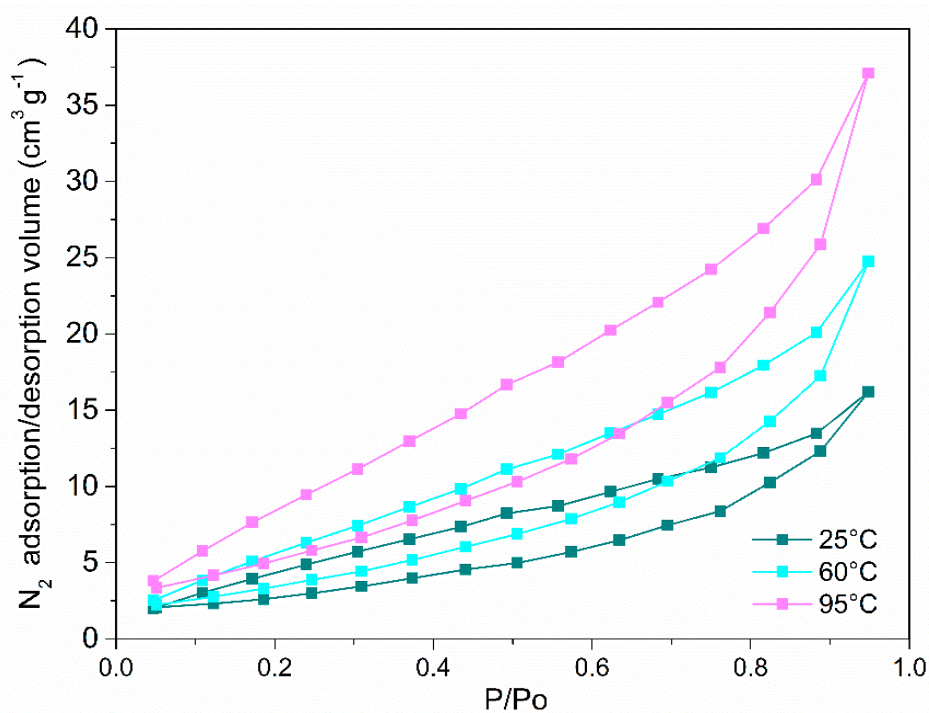


Figure 6. Adsorption/desorption isotherms of as-deposited C(OH)_2 at 25, 60, and 95 °C.

The specific surface area was calculated by Brunauer–Emmett–Teller (BET) calculation; the results are listed in Table 3. A proportional increment in the calculated area with electrodeposit temperature is associated with higher ion mobility of the Co^{2+} during the electrodeposition process, promoting major nucleation sites for the crystal structures of $\beta\text{-Co(OH)}_2$ to form smaller pores which can increment the surface area. The specific area obtained through BET calculations are much lower than those reported by Aghazadeh et al. [20], close to $100 \text{ m}^2 \text{ g}^{-1}$ for similar powder compounds. The difference in specific area arises from the electrodeposition process, which was carried out without pH buffer, unlike the work of Aghazadeh, where the generation of OH^- groups was promoted by a pH mediator used in the synthesis. According to the Barrett–Joyner–Halenda (BJH) pore size calculation, the distribution was observed in the range of 20 and 50 Å. Finally, an electrodeposited sample at 95 °C adsorbed a greater amount of N_2 , compared to the other two samples (25 and 60 °C); the increase in the adsorption volume can be explained due to the smaller size of the metal hydroxide obtained.

Table 3. The specific surface area of as-deposited materials.

Sample	Specific Surface Area ($\text{m}^2 \text{ g}^{-1}$)
25 °C	9.11
60 °C	10.04
95 °C	30.41

3.2. Electrochemical Characterization: Three-Electrode Cell Configuration

Figure 7 shows the voltammograms of the electrodeposits made at the three synthesis temperatures of 25, 60, and 95 °C, with a scan rate of 20 mV s^{-1} and using 1M KOH as the electrolyte. The material that shows the highest current density was the electrodeposit synthesized at 25 °C. This current can be associated with two factors related to EDX analyses and the growth mechanism involved during electrodeposition. According to the EDX analysis, when electrodepositing was performed at 25 °C, a higher content of atomic oxygen was observed. Regarding the nucleation of Co(OH)_2 at lower temperatures, it tends to form more massive clusters, as observed in the results by SEM (Figure 4—25 °C).

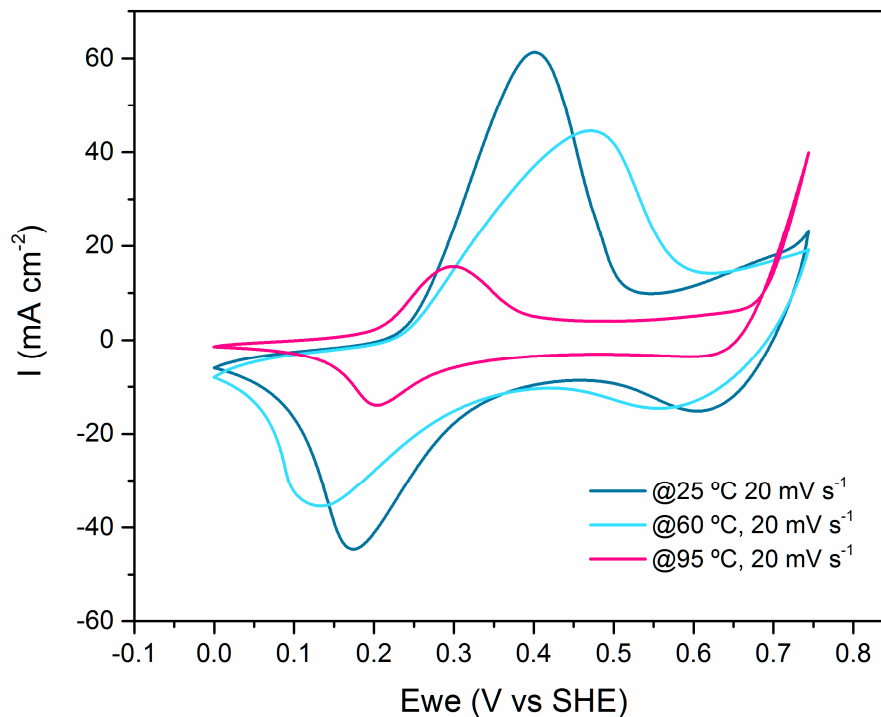
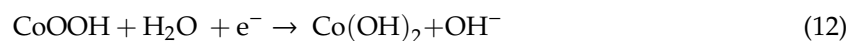
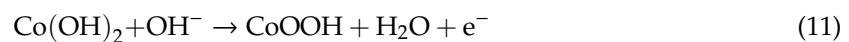


Figure 7. Cyclic voltammograms of $\text{Co}(\text{OH})_2$ from 0 to 0.7 V vs. Standard Hydrogen Electrode (SHE) at a scan rate of 20 mV s^{-1} in 1 M KOH.

It is worth mentioning that the appearance of redox signals can be described as a quasi-reversible process due to the displacement of the redox signal in the evaluated materials, although, for the $95 \text{ }^\circ\text{C}$ as-deposited material, it can be seen that the oxygen evolution reaction (OER) occurs, increasing the response current in the Cyclic Voltammogram (CV) profile. The oxidation of $\text{Co}(\text{OH})_2$ to CoOOH —reaction (11)—and the reduction of CoOOH to cobalt hydroxide, as shown in reaction (12), increases the electron transfer in the $95 \text{ }^\circ\text{C}$ as-deposited material.



In the cyclic voltammetry analysis, the difference in response currents can be associated with oxygen content in the as-deposited material, since the $25 \text{ }^\circ\text{C}$ as-deposited material presents a more prominent cluster structure, according to SEM and EDX analysis. Equation (13) was used to calculate the specific charge.

$$Q = \frac{1}{m A v} \int_{V_{cp}}^{V_{ap}} I(V) dV \quad (13)$$

where Q , is the specific charge (C h g), m is the deposited mass of the electrode with a calculated value of 0.7 mg cm^{-2} , A corresponds to the area of the electrode equal to 16 cm^2 , v corresponds to the scan rate (V s^{-1}), and the integral of $I(V) dV$ equals the area under the curve for the oxidation (V_{ap}) and reduction (V_{cp}) peaks. The specific charge values obtained were 25.64 , 24.78 , and 9.44 C h g^{-1} for the three electrodeposits made at synthesis temperatures of 25 , 60 , and $95 \text{ }^\circ\text{C}$, respectively.

Recent progress on electrochemical energy storage aims at a standardization method to report energy-storage units for a specific type of material according to the storage mechanism in which they predominantly work, as mentioned by Balducci et al. [30]. The energy metrics of materials tested in a half-cell configuration seeks to present the electrochemical behavior of this battery type of materials in which Faradic contribution in the storage mechanism plays a significant role. Since the Faradic

contribution arises in this case from potential dependent redox according to reactions (5) and (6), since Faradic contributions presented in redox materials tend to behave more like a battery-type, the difference and outlooks to choose between a capacity or capacitance measures is suggested [31].

Since redox activity was presented, cyclability tests were performed by subjecting the material to 500 cycles with a scan rate of 20 mV s^{-1} in a potential window of 0 to 0.7 V vs. SHE in 1M KOH electrolytic solution. The response currents in the cyclic voltammetry decreased by 45%, 22%, and 24% for the synthesis temperatures of 25, 60 and 95 °C, respectively, after 500 cycles. The decrease in charge retention is associated with possible irreversible intercalation phenomena of K^+ ions in the laminar structure of $\text{Co}(\text{OH})_2$ at the electrode–electrolyte interface.

Quasireversible Faradic processes were carried out so that the oxygen content in the sample is inversely proportional to the electrochemical stability determined by scanning cycles. Table 4 lists the calculated areal capacity values for the three as-deposited electrodes at electrochemical synthesis temperatures of 25, 60 and 95 °C through 500 voltammetric cycles at a constant scan rate of 20 mV s^{-1} . The highest areal capacity was obtained in the 25 °C electrode material with a value of $27.82 \text{ mA h cm}^{-2}$. The as-deposited material at 60 °C presented the more stable performance, with an average areal capacity of $23.61 \text{ mA h cm}^{-2}$.

Table 4. The areal capacity for three-electrode configuration mA h cm^{-2} .

Cycle	Areal Capacity (mA h cm^{-2})		
	25 °C	60 °C	95 °C
1	27.82	26.88	10.24
100	23.47	25.32	9.38
200	21.29	23.65	8.53
300	19.56	22.62	8.16
400	18.25	22.10	7.73
500	17.37	21.08	7.56

Meanwhile, the 95 °C as-deposited electrode shows the lowest areal capacity of $10.24 \text{ mA h cm}^{-2}$, with a small difference in the last cycle of $7.56 \text{ mA h cm}^{-2}$. The areal capacity drop is associated with the quasi-reversible-type redox pair of the electrodeposited material during ion intercalation in the voltammetric cycling process [31].

3.3. Electrochemical Performance of ECs

Voltammograms of the two-electrode cell symmetrical arrangement with $\text{Co}(\text{OH})_2$ electrodeposited electrodes at three different syntheses are shown in Figure 8. The voltammogram corresponding to the material electrodeposited at 25 °C (Figure 8a) does not present notorious oxidation–reduction signals compared with the three electrochemical cells, which may suggest that cell configuration influences the response current and the storage process is carried out mainly by electromagnetic contributions with minor Faradic contributions [32]. The recorded current density presents an increment above 0.6 V, this increment is related to the Faradic contribution of $\text{Co}(\text{OH})_2$ by oxidation. In contrast to when the EC undergoes oxidation in the voltammogram, the reduction portion shows small current contributions, according to the semi-rectangular shape related to the reduction of CoOOH into $\text{Co}(\text{OH})_2$. The voltammogram for the symmetric as-deposited EC at 60 °C (Figure 8b) presented a smaller oxidation current increase after 0.6 V, which may occur due to the higher reversibility of the as-deposited material at that specific temperature. No considerable changes in the voltammogram shape of as-deposited EC at 60 °C, are observed when the scan rate is increased; this may suggest a low equivalent series resistance (ESR). Finally, in Figure 8c, the as-deposited EC at 95 °C voltammogram is presented, showing a higher current response—reaching a current response close to 400 mA cm^{-2} when the EC was evaluated at the maximum scan rate of 100 mV s^{-1} . However, in the cathodic portion of the voltammogram, the current response is less pronounced, compared with the lower-temperature

as-deposited EC of 25 and 60 °C. The difference can be attributed to the interlaminar space, as mentioned in the morphology characterization section; there is a change in the size of the as-deposited materials as the temperature was increased, reducing the size of the as-deposited materials.

In Figure 8d, a series of charge/discharge profiles is presented at a constant current density of 12.5 mA cm^{-2} given by the cyclic voltammetry analysis. The charge/discharge galvanostatic profile of the ECs is presented in Figure 8d. The profile exhibited typical plateaus in samples at 60 and 95 °C. The fin's shape can indicate a charge-storage mechanism with Faradic contributions since a regular triangular profile can be observed in a double-layer charge mechanism. ECs at 60 °C presented the most significant charge/discharge profile of 33 s, nearly three-times the exhibited time of ECs at 25 °C. The differences arise in the material composition since the Co increases with temperature, as shown in the EDX analysis (Table 2), leading to an increase in the charge transfer through the oxidation–reduction process.

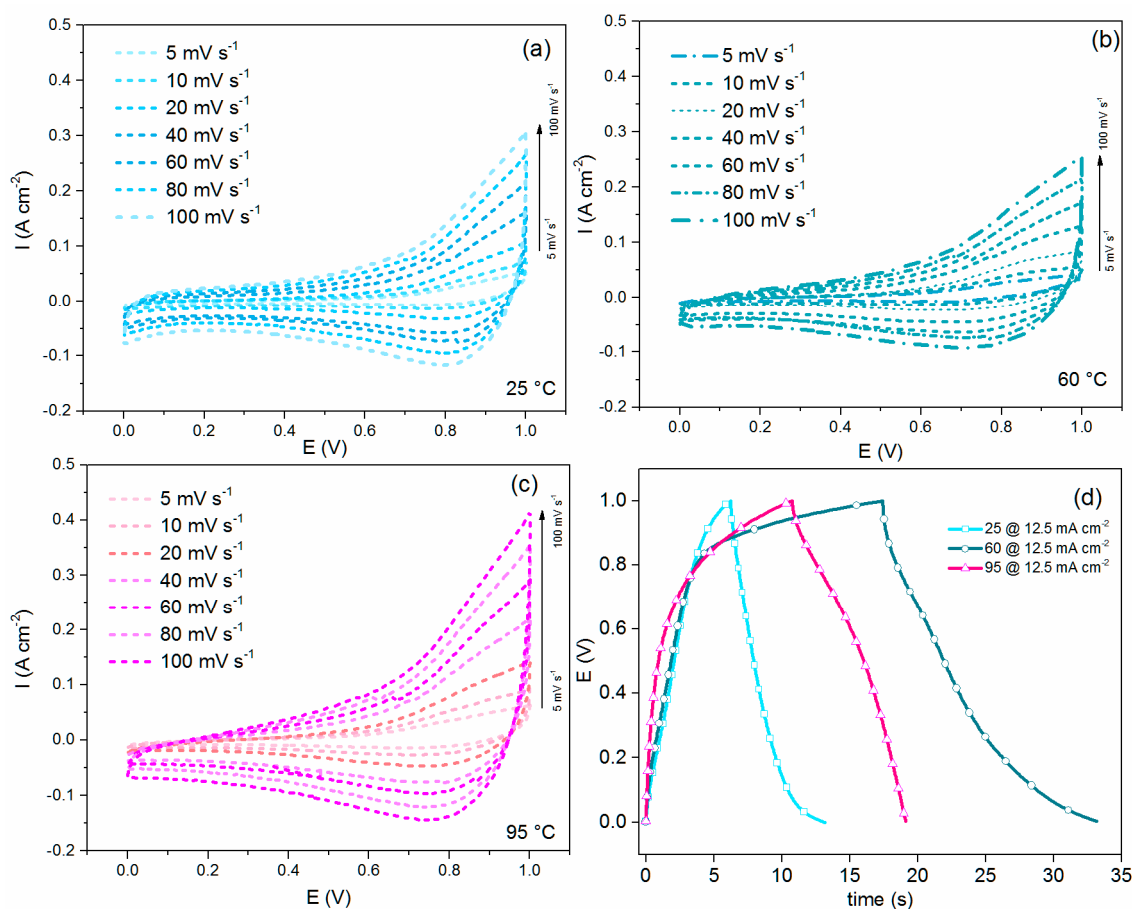


Figure 8. Voltammogram of the symmetric electrochemical cell (EC) as-deposited at (a) 25 °C, (b) 60 °C, (c) 95 °C and (d) galvanostatic charge/discharge profiles of the different ECs at a current density of 12.5 mA cm^{-2} .

Areal capacity profile curves across the charge density in the charge/discharge process are shown in Figure 9a. The profiles exhibited a reduction of areal capacity when the charge density increased. Between the as-deposited materials, the 25 °C as-deposited EC presented the lowest areal capacity of $1.97 \text{ mA h cm}^{-2}$ but maintained nearly 60% of the maximum capacity through to the end of the charge/discharge current density range, with a value of $1.124 \text{ mA h cm}^{-2}$.

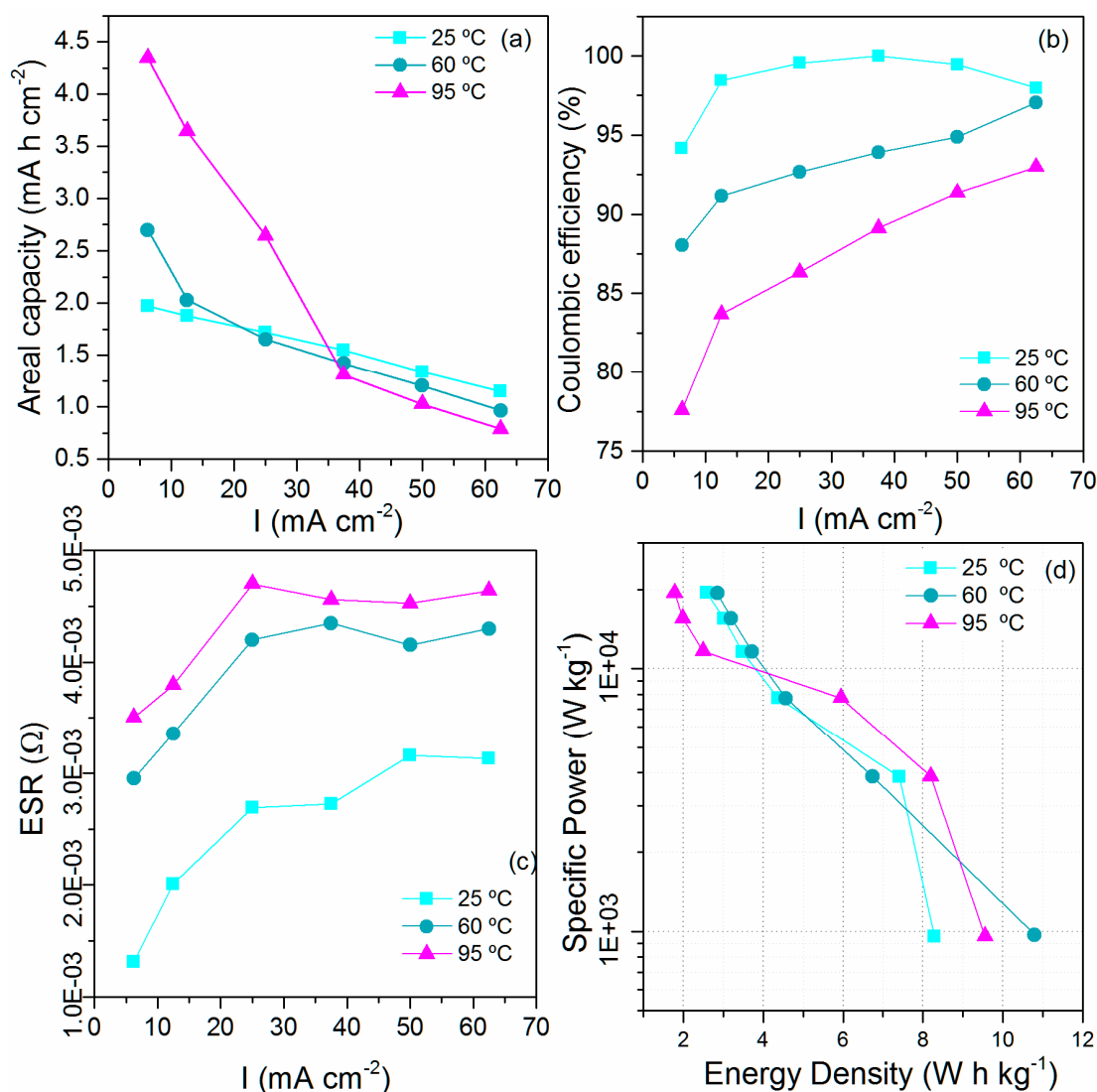


Figure 9. (a) Areal capacity distribution; (b) coulombic efficiency of ECs; (c) ESR of ECs; and (d) Ragone plot for the electrochemical performance of symmetrical ECs.

Unlike the as-deposited EC synthesized at 60 °C, which shows an increase of the initial areal capacity of 2.70 mA h cm⁻² at lowest current density charge/discharge at 6.25 mA cm⁻², the EC profile shows a lower retention of the capacity when the EC increases the current density with a 65% areal capacity drop at the maximum charge/discharge current density of 62.5 mA cm⁻². EC as-deposited at 95 °C reached the maximum areal capacity recorded at 6.25 mA cm⁻² of 4.37 mA h cm⁻² but presented the highest areal capacity decrease of the three samples of 85%. The decrease in the areal capacity can be associated with the rate of charge/discharge and the internal structure of the LDH, in which the lower rate charge/discharge was favored by slow insertion and desorption of the ions in the charge process.

Moreover, the pseudocapacitance, as a conjugated phenomenon in which the double-layer storage mechanism and the Faradic contribution through redox reaction, adsorption/desorption, and ion intercalation can take place at the same time in the charge-storage mechanism [33]. Along with this, the changes in the material upon oxidation must be taken into account; as reported in the literature, α -Co(OH)₂ is not stable in alkaline media and undergoes a transition to β -phase [34], this can be associated with the ion insertion and the interplanar broadening of the lamellar structure.

Coulombic efficiency evaluation (shown in Figure 9b) presented controlled behavior through the charge densities interval. EC at 95 °C exhibits the highest-efficiency EC with an increase at low currents due to activation of the material, followed by a fast ion adsorption/desorption process when

the current charge is increased, reaching 98% efficiency at the maximum current density of 62.5. For the ECs as deposited at 60 and 95 °C, the efficiency performance is lower, this reduction is attributed to the decreased interlaminar space, as shown by XRD analysis, hindering the insertion of the electrolyte in the mesoporous structures.

Despite the decrease in the coulombic efficiency, the presented efficiencies exceed 80%. In Figure 9c, the ECs present the equivalent series resistance (ESR) of the as-deposited ECs. EC at 95 °C reached a maximum value of 5 mΩ; this resistance value agrees with the low Ohmic drop as seen in Figure 8d charge/discharge profile. However, it is noteworthy that the increase in the resistance when the current increases can be attributed to the oxidation process by the quasi-reversible deposited material, which, upon being exposed to high potential, forces the oxygen evolution reaction, increasing the electric resistance in the oxidized material.

The Ragone plot in Figure 9d presents the energy density and power output of the ECs. The presented behavior across the current density can be described as a two-type behavior: when ECs are charged with low current densities, the device exhibits a high-energy-density response, this can be explained by the slow rate of the charge transfer process in the charge/discharge stage, resulting in a slower ion insertion/desorption process; when the current density increases, this ion insertion/desorption is accelerated.

Furthermore, the second type of behavior can be described as an affinity to a high-power output for EC when it is charged at the highest current density in the range, presenting up to 19 kW kg⁻¹. From the obtained results, it can be confirmed that the effect of temperature affects the morphology and, thus, varies the electrochemical performance of the ECs. In comparison with a similar EC cell arrangement and material, the results obtained are higher than those reported by Jagadale et al., with an energy density of 3.96 W h kg⁻¹ (areal capacity of 1.35 mA h cm⁻²) for a similar electrochemical cell based on thin-layer electrodes of Co(OH)₂ [19].

Through electrochemical impedance spectroscopy analysis, the electrochemical resistance of ECs was evaluated; in Figure 10, Nyquist plots are presented. The spectra show a deviation from the behavior of an electrochemical capacitor, which can be represented as a vertical line with a phase angle of 90° [35]. However, a deviation from the vertical line in pure capacitors is observed, and this is associated with diffusion resistance [36]. As can be seen, there is no semicircle area in the high-frequency region, which can be attributed to the low charge transfer resistance of the material [37]. The increase in resistance is attributed to the pore reduction in the materials.

From the experimentally obtained values, an equivalent circuit was determined, which is presented in the inset in Figure 10b. This circuit was adjusted using the Zview[®] software (Scribner Associates Inc., Southern Pines, NC, USA). The circuit is composed of three elements. Table 5 shows the values obtained from the proper circuit adjustment of the experimental data.

The obtained values of ESR are in the range of 77 to 84 mΩ for the electrochemical capacitors. These values are slightly higher than those presented in the previous section of the galvanostatic evaluation. As the equivalent circuit information shows, the first element L₁ corresponds to an inductor element, the nature of this element can be associated with the cable connections in the apparatus between the EC and potentiostat, yielding a small inductance contribution. The second element corresponds to a resistor element R₁ in the equivalent circuit, and it can be described as the equivalent series resistance (ESR), which corresponds to the sum of the resistances of the components present in the electrochemical system. The third element corresponds to a series-connected constant phase element CPE₁, and the element is composed of two sub-elements, the transfer element CPE₁-T and the phase angle represented by the CPE₁-P subcomponent; deviations from a 90° angle suggest that a Faradic contribution can be seen in the high-frequency region. Finally, a parallel-connected resistor R₂ element is shown. The resistance at the low-frequency region can be attributed to the charge transfer process, reaching a maximum value of 33.57 Ω for the 95 °C EC.

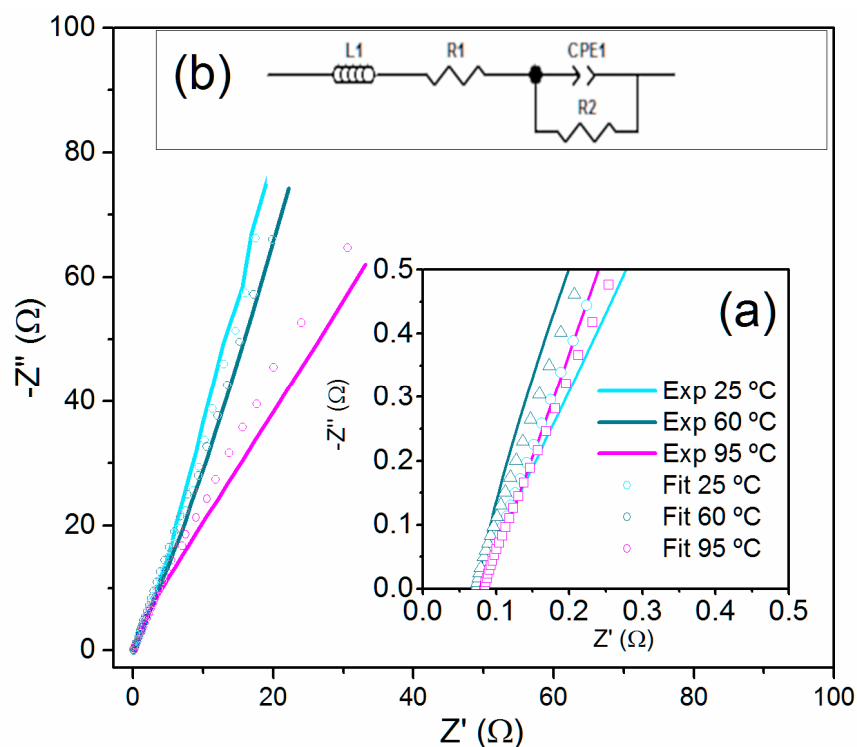


Figure 10. Nyquist diagram for the symmetrical EC at different synthesis temperatures: (a) high-frequency region; (b) equivalent circuit for the fitted experimental data.

Table 5. Experimental data of potentiostatic electrochemical impedance spectroscopy (PEIS) fixed data.

EC-Co(OH) ₂	L ₁	R ₁ (Ω)	CPE ₁ -T	CPE ₁ -P	R ₂ (Ω)	χ ²
25 °C	1.32 × 10 ⁻⁷	7.90 × 10 ⁻²	3.86 × 10 ⁻³	0.77	19.42	3.08 × 10 ⁻³
60 °C	1.34 × 10 ⁻⁷	7.76 × 10 ⁻²	2.86 × 10 ⁻³	0.76	22.54	5.48 × 10 ⁻³
95 °C	1.39 × 10 ⁻⁷	8.48 × 10 ⁻²	4.26 × 10 ⁻³	0.70	33.57	6.82 × 10 ⁻³

4. Conclusions

Electrochemical deposition of Co(OH)₂ was achieved without the use of any surfactant or pH buffer in the synthesis, which simplifies the synthesis process. As morphological studies suggest, the changes in the temperature bath lead to different microstructures, with variations in the crystalline structure, as suggested by the XRD analysis. The increase in the temperature bath to 95 °C leads to the formation of a mixed-phase compound, comprising both α-Co(OH)₂ and β-Co(OH)₂ phases. According to XRD analysis, the deposited material has a reduced laminar space, which limits the ion intercalation, as shown by the electrochemical characterization. The study of the effect on the electrochemical properties showed that the electrosynthesis temperature solution of 60 °C offers desirable deposition conditions in terms of the evaluated response analyzed by physicochemical, morphological, textural, and electrochemical characterization. An areal capacity value of 2.02 mA h cm⁻² was calculated in a two-electrode cell when evaluated at a current density of 12.5 mA cm⁻² for the 60 °C as-deposited material, which means that, in this study, a “mild temperature” appears to be favorable for the electrodeposition process in the preparation of metal hydroxides for its incorporation in a base matrix of a composite material for energy-storage applications.

Author Contributions: Conceptualization, V.P.-E. and D.E.P.-C.; methodology, V.P.-E. and J.M.B.-L.; formal analysis, V.P.-E., A.K.C.-G. and B.E.-M.; investigation, V.P.-E.; resources, D.E.P.-C.; data analysis, V.P.-E.; writing—original draft preparation, V.P.-E., A.K.C.-G., B.E.-M., and D.E.P.-C.; writing—review and editing, A.K.C.-G. and B.E.-M.; supervision, D.E.P.-C. and J.A.U.-C.; project administration, D.E.P.-C.; funding acquisition, D.E.P.-C.

Funding: This work was supported by CONACYT (Mexico) CB 2011-166356 project fund, SENER Sust. No. 254667; CONACYT student grant (362308) and Doctoral trainees grant by CICY.

Acknowledgments: V.P.-E. acknowledges the technical support from M. Baas-López, J. Domínguez-Maldonado, T. Toledano-Thompson, and E. Escobedo-Hernández from CICY for the technical support in material characterization by physisorption and textural characterization, FT-IR, SEM and electrochemical experimentation respectively.

Conflicts of Interest: The authors declare no conflict of interest and declare that the funders had no role in the design of the study; in the collection, analyses, or interpretation of data; in the writing of the manuscript, or in the decision to publish the results.

References

1. Partridge, J.; Abouelamaimen, D.I. The role of supercapacitors in regenerative braking systems. *Energies* **2019**, *12*, 2683. [[CrossRef](#)]
2. Kötz, R.; Carlen, M. Principles and applications of electrochemical capacitors. *Electrochim. Acta* **2000**, *45*, 2483–2498. [[CrossRef](#)]
3. Rudge, A.; Raistrick, I.; Gottesfeld, S.; Ferraris, J.P. A study of the electrochemical properties of conducting polymers for application in electrochemical capacitors. *Electrochim. Acta* **1994**, *39*, 273–287. [[CrossRef](#)]
4. Cottineau, T.; Toupin, M.; Delahaye, T.; Brousse, T.; Belanger, D. Nanostructured transition metal oxides for aqueous hybrid electrochemical supercapacitors. *Appl. Phys. A* **2006**, *82*, 599–606. [[CrossRef](#)]
5. Parra-Elizondo, V.; Escobar-Morales, B.; Morales, E.; Pacheco-Catalán, D. Effect of carbonaceous support between graphite oxide and reduced graphene oxide with anchored CO_3O_4 microspheres as electrode-active materials in a solid-state electrochemical capacitor. *J. Solid State Electrochem.* **2017**, *21*, 975–985. [[CrossRef](#)]
6. Cheng, J.; Zhang, J.; Liu, F. Recent development of metal hydroxides as electrode material of electrochemical capacitors. *RSC Adv.* **2014**, *4*, 38893–38917. [[CrossRef](#)]
7. Yedluri, A.K.; Araveeti, E.R.; Kim, H.J. Facilely synthesized $\text{NiCo}_2\text{O}_4/\text{NiCo}_2\text{O}_4$ nanofile arrays supported on nickel foam by a hydrothermal method and their excellent performance for high-rate supercapacitance. *Energies* **2019**, *12*, 1308. [[CrossRef](#)]
8. Kumar, Y.A.; Kim, H.-J. Effect of time on a hierarchical corn skeleton-like composite of coo@zno as capacitive electrode material for high specific performance supercapacitors. *Energies* **2018**, *11*, 3285. [[CrossRef](#)]
9. Louloudakis, D.; Vernardou, D.; Spanakis, E.; Katsarakis, N.; Koudoumas, E. Electrochemical properties of vanadium oxide coatings grown by apcvd on glass substrates. *Surf. Coat. Technol.* **2013**, *230*, 186–189. [[CrossRef](#)]
10. Vernardou, D.; Apostolopoulou, M.; Louloudakis, D.; Katsarakis, N.; Koudoumas, E. Hydrothermally grown $\beta\text{-V}_2\text{O}_5$ electrode at 95°C . *J. Colloid Interface Sci.* **2014**, *424*, 1–6. [[CrossRef](#)]
11. Ghosh, S.; Polaki, S.; Sahoo, G.; Jin, E.-M.; Kamruddin, M.; Cho, J.S.; Jeong, S.M. Designing metal oxide-vertical graphene nanosheets structures for 2.6 v aqueous asymmetric electrochemical capacitor. *J. Ind. Eng. Chem.* **2019**, *72*, 107–116. [[CrossRef](#)]
12. Miller, J.R.; Burke, A.F. Electrochemical capacitors: Challenges and opportunities for real-world applications. *Electrochem. Soc. Interface* **2008**, *17*, 53.
13. Ingole, R.; Fugare, B.; Lokhande, B. Ultrahigh specific capacitance of spray deposited nanoporous interconnected ruthenium oxide electrode fabric for supercharged capacitor. *J. Mater. Sci. Mater. Electron.* **2017**, *28*, 16374–16383. [[CrossRef](#)]
14. Elumalai, P.; Vasan, H.N.; Munichandraiah, N. Electrochemical studies of cobalt hydroxide—An additive for nickel electrodes. *J. Power Sources* **2001**, *93*, 201–208. [[CrossRef](#)]
15. Hou, Y.; Kondoh, H.; Shimojo, M.; Kogure, T.; Ohta, T. High-yield preparation of uniform cobalt hydroxide and oxide nanoplatelets and their characterization. *J. Phys. Chem. B* **2005**, *109*, 19094–19098. [[CrossRef](#)]
16. Hu, Z.; Mo, L.; Feng, X.; Shi, J.; Wang, Y.; Xie, Y. Synthesis and electrochemical capacitance of sheet-like cobalt hydroxide. *Mater. Chem. Phys.* **2009**, *114*, 53–57. [[CrossRef](#)]
17. Li, Y.; Chen, Q. Electrodeposition of $\text{Co}(\text{OH})_2$ film and its conversion into CO_3O_4 film for supercapacitors. *Asian J. Chem.* **2012**, *24*, 4736–4740.
18. Gupta, V.; Kusahara, T.; Toyama, H.; Gupta, S.; Miura, N. Potentiostatically deposited nanostructured $\alpha\text{-Co}(\text{OH})_2$: A high performance electrode material for redox-capacitors. *Electrochem. Commun.* **2007**, *9*, 2315–2319. [[CrossRef](#)]

19. Jagadale, A.D.; Kumbhar, V.S.; Dhawale, D.S.; Lokhande, C.D. Performance evaluation of symmetric supercapacitor based on cobalt hydroxide [Co(OH)₂] thin film electrodes. *Electrochim. Acta* **2013**, *98*, 32–38. [[CrossRef](#)]
20. Aghazadeh, M.; Shiri, H.M.; Barmi, A.-A.M. Uniform β-Co(OH)₂ disc-like nanostructures prepared by low-temperature electrochemical route as an electrode material for supercapacitors. *Appl. Surf. Sci.* **2013**, *273*, 237–242. [[CrossRef](#)]
21. Zhou, W.-J.; Zhao, D.-D.; Xu, M.-W.; Xu, C.-L.; Li, H.-L. Effects of the electrodeposition potential and temperature on the electrochemical capacitance behavior of ordered mesoporous cobalt hydroxide films. *Electrochim. Acta* **2008**, *53*, 7210–7219. [[CrossRef](#)]
22. Malek Barmi, A.-A.; Aghazadeh, M.; Arhami, B.; Shiri, H.M.; Fazl, A.A.; Jangju, E. Porous cobalt hydroxide nanosheets with excellent supercapacitive behavior. *Chem. Phys. Lett.* **2012**, *541*, 65–69. [[CrossRef](#)]
23. Sobha Jayakrishnan, D. Electrodeposition: The versatile technique for nanomaterials. In *Corrosion Protection and Control Using Nanomaterials*; Saji, V.S., Cook, R., Eds.; Woodhead Publishing: Sawston/Cambridge, UK, 2012; pp. 86–125.
24. Wang, L.; Fu, J.; Zhang, Y.; Liu, X.; Yin, Y.; Dong, L.; Chen, S. Mesoporous β-Co(OH)₂ nanowafers and nanohexagonals obtained synchronously in one solution and their electrochemical hydrogen storage properties. *Prog. Nat. Sci. Mater. Int.* **2016**, *26*, 555–561. [[CrossRef](#)]
25. Liu, Z.; Ma, R.; Osada, M.; Takada, K.; Sasaki, T. Selective and controlled synthesis of α- and β-cobalt hydroxides in highly developed hexagonal platelets. *J. Am. Chem. Soc.* **2005**, *127*, 13869–13874. [[CrossRef](#)]
26. Dam, D.T.; Lee, J.-M. Ultrahigh pseudocapacitance of mesoporous ni-doped Co(OH)₂/ITO nanowires. *Nano Energy* **2013**, *2*, 1186–1196. [[CrossRef](#)]
27. Kong, L.-B.; Lang, J.-W.; Liu, M.; Luo, Y.-C.; Kang, L. Facile approach to prepare loose-packed cobalt hydroxide nano-flakes materials for electrochemical capacitors. *J. Power Sources* **2009**, *194*, 1194–1201. [[CrossRef](#)]
28. Aghazadeh, M.; Dalvand, S.; Hosseini-fard, M. Facile electrochemical synthesis of uniform β-Co(OH)₂ nanoplates for high performance supercapacitors. *Ceram. Int.* **2014**, *40*, 3485–3493. [[CrossRef](#)]
29. Brownsona, J.R.; Lévy-Clément, C. Nanostructured α and β-cobalt hydroxide thin films. *Electrochim. Acta* **2009**, *54*, 6637–6644. [[CrossRef](#)]
30. Balducci, A.; Belanger, D.; Brousse, T.; Long, J.W.; Sugimoto, W. Perspective—A guideline for reporting performance metrics with electrochemical capacitors: From electrode materials to full devices. *J. Electrochem. Soc.* **2017**, *164*, A1487–A1488. [[CrossRef](#)]
31. Ulaganathan, M.; Maharjan, M.M.; Yan, Q.; Aravindan, V.; Madhavi, S. B-Co(OH)₂ nanosheets: A superior pseudocapacitive electrode for high-energy supercapacitors. *Chem. Asian J.* **2017**, *12*, 2127–2133. [[CrossRef](#)]
32. Khomenko, V.; Frackowiak, E.; Béguin, F. Determination of the specific capacitance of conducting polymer/nanotubes composite electrodes using different cell configurations. *Electrochim. Acta* **2005**, *50*, 2499–2506. [[CrossRef](#)]
33. Munoz-Rojas, D.; Moya, X. *Materials for Sustainable Energy Applications: Conversion, Storage, Transmission, and Consumption*; Pan Stanford Publishing Pte. Ltd.: Singapore, 2016.
34. Hsu, Y.-K.; Chen, Y.-C.; Lin, Y.-G. Characteristics and electrochemical performances of lotus-like CuO/Cu(OH)₂ hybrid material electrodes. *J. Electroanal. Chem.* **2012**, *673*, 43–47. [[CrossRef](#)]
35. Pacheco, D.; Smith, M.; Morales, E. Characterization of composite mesoporous carbon/conducting polymer electrodes prepared by chemical oxidation of gas-phase absorbed monomer for electrochemical capacitors. *Int. J. Electrochem. Sci.* **2011**, *6*, 78–90.
36. Prabakaran, S.R.; Vimala, R.; Zainal, Z. Nanostructured mesoporous carbon as electrodes for supercapacitors. *J. Power Sources* **2006**, *161*, 730–736. [[CrossRef](#)]
37. Tehare, K.K.; Zate, M.K.; Navale, S.T.; Bhande, S.S.; Gaikwad, S.L.; Patil, S.A.; Gore, S.K.; Naushad, M.; Alfadul, S.M.; Mane, R.S. Electrochemical supercapacitors of cobalt hydroxide nanoplates grown on conducting cadmium oxide base-electrodes. *Arab. J. Chem.* **2017**, *10*, 515–522. [[CrossRef](#)]

